Cancer Research

IFNγ PET Imaging as a Predictive Tool for Monitoring Response to Tumor Immunotherapy

Heather M. Gibson[1], Brooke N. McKnight[1], Agnes Malysa[1], Greg Dyson[1], Wendy N. Wiesend[2], Claire E. McCarthy[1], Joyce Reyes[1], Wei-Zen Wei[1], and Nerissa T. Viola-Villegas[1]

Abstract

IFNγ is an attractive target for imaging active antitumor immunity due to its function in the T-cell signaling axis. Here, we test an IFNγ immuno-PET (immunoPET) probe for its capacity to identify adaptive immunotherapy response after HER2/neu vaccination in both spontaneous salivary and orthotopic neu$^+$ mouse mammary tumors. IFNγ immunoPET detected elevated cytokine levels *in situ* after vaccination, which inversely correlated with tumor growth rate, an indicator of response to therapy. In a model of induced T-cell anergy where CD8 T cells infiltrate the tumor, but upregulate PD-1, IFNγ tracer uptake was equivalent to isotype control, illustrating a lack of antitumor T-cell activity. The IFNγ immunoPET tracer detected IFNγ protein sequestered on the surface of tumor cells, likely in complex with the IFNγ receptor, which may explain imaging localization of this soluble factor *in vivo*. Collectively, we find that the activation status of cytotoxic T cells is annotated by IFNγ immunoPET, with reduced off-target binding to secondary lymphoid tissues compared with imaging total CD3$^+$ tumor-infiltrating lymphocytes. Targeting of soluble cytokines such as IFNγ by PET imaging may provide valuable noninvasive insight into the function of immune cells *in situ*.

Significance: This study presents a novel approach to monitor therapeutic outcomes via IFNγ-targeted positron emission tomography. *Cancer Res; 78(19); 5706–17. ©2018 AACR.*

Introduction

During adaptive immunotherapy (ITx), activated T cells infiltrating the tumor are often the principal components of treatment providing a "search-and-destroy" mechanism through specific recognition of tumor-associated antigens (TAA; refs. 1, 2). Recent emerging tumor-targeted ITx strategies are met with positive and durable outcomes in a subset of patients; however, many remain nonresponsive, exposing a strong urgency for consistent methods to monitor therapeutic response in a timely manner (3). Peripheral immune monitoring assays are often restricted to one antigen, are nonstandardized, and may not reflect the dynamic activity occurring within the tumor (4, 5). Posttreatment biopsy can be used to evaluate tumor infiltrates (6); however, tumor heterogeneity and general accessibility may affect the adequacy and/or feasibility of this approach (7). Image-guided focal analysis of intratumoral immune activity may eliminate these issues by providing noninvasive, real-time efficacy predictions *in situ*. To date, ITx PET tracer development has focused on immune cell surface molecule detection, particularly against CD3 (8) and CD8 (9). Others have developed tracers targeting immune checkpoint molecules PD-1/PD-L1 (10–15) to help identify candidate patients for checkpoint blockade therapy. These probes are limited, however, as they do not mark functional downstream effector tumoricidal activity.

The cytokine IFNγ is predominantly produced by activated Type 1 T helper (Th1)–skewed CD4 T cells, cytotoxic CD8 T cells (CTL), and both natural killer (NK) and NKT cells (16). Both Th1 and CTL contribute to antigen-specific tumor cell recognition and destruction, which is particularly advantageous in the context of immunotherapeutic approaches including checkpoint blockade, adoptive cell therapies, and vaccination (17–19). IFNγ signaling contributes to tumor cell killing by a variety of mechanisms including upregulation of Fas/FasL and MHC molecules (20, 21); however, tumor expression of PD-L1 is also positively regulated by IFNγ signaling, which ultimately serves as a feedback mechanism to quell immune activation.

The focus of our study underscores the development of an mAb PET tracer targeting IFNγ. We show that IFNγ PET associates with response to ITx. Tumors treated with TAA DNA vaccination show increased IFNγ detection coupled with an influx of T cells. The level of IFNγ uptake inversely correlates with tumor growth rate. Alternatively, in a model of induced T-cell exhaustion, we find T cells infiltrate but fail to produce detectable IFNγ as measured by PET imaging. We further demonstrated that IFNγ PET provides consistent sensitivity for the detection of ITx response when compared with antigen-specific peripheral immune monitoring. Collectively, IFNγ PET may serve as a noninvasive, comprehensive approach to the evaluation of tumor ITx.

[1]Department of Oncology, Karmanos Cancer Institute, Detroit, Michigan. [2]Department of Anatomic Pathology, Beaumont Health System, Royal Oak, Michigan.

Note: Supplementary data for this article are available at Cancer Research Online (http://cancerres.aacrjournals.org/).

H.M. Gibson and B.N. McKnight contributed equally to this article.

Corresponding Authors: Nerissa T. Viola-Villegas, Karmanos Cancer Institute, 4100 John R Street, Detroit, MI 48201. Phone: 313-576-8309; Fax: 313-576-8928; E-mail: villegan@karmanos.org; and Wei-Zen Wei, Departments of Immunology/Microbiology and Oncology, 421 E. Canfield Street, Suite 2226, Detroit, MI 48201-2013. Phone: 313-578-4651; E-mail: weiw@karmanos.org

doi: 10.1158/0008-5472.CAN-18-0253

Materials and Methods

Mice

Female BALB/c mice (6–8 weeks old) were purchased from Charles River Laboratories. Heterozygous BALB/NeuT (NeuT) mice were bred in-house. NeuT male mice, which express a transforming rat *neu*, develop atypical ductal hyperplasia in 1 to 2 parotid glands by 6 weeks of age, which progresses to multifocal acinic cell adenocarcinoma *in situ* at approximately 19 weeks of age (22). All animal procedures were approved by and performed in accordance with the regulation of Wayne State University Institutional Animal Care and Use Committee.

Radiochemistry

All antibodies were obtained from eBioscience, whereas the nonspecific IgG isotype controls were purchased from Jackson ImmunoResearch and Thermo Fisher unless otherwise stated. Chelators were obtained from Macrocyclics. Radioisotopes were obtained from 3D Imaging, LLC. Synthesis of ^{89}Zr-anti-CD3, ^{89}Zr-anti-IFNγ, and nonspecific ^{89}Zr-anti-IgG followed established protocols (23, 24). Briefly, p-SCN-Bn-Desferrioxamine (DFO, Macrocyclics) was incubated with 145-2C11 (anti-CD3ε, Armenian hamster, IgG; eBioscience) or AN-18 (anti-IFNγ, rat IgG1, kappa; eBioscience) at a ratio of 1:5 (Ab:DFO) in PBS at pH of 9 for 1 hour at 37°C and purified via centrifugation with a molecular weight column filter (MWCO: 30 kDa; GE Vivaspin 500). Facile ^{89}Zr-radiolabeling (3D Imaging) of the 145-2C11-DFO or AN-18-DFO conjugates proceeded in a neutral pH environment in saline at room temperature after 1 hour of incubation. Unbound ^{89}Zr ($t_{1/2}$ = 3.27 days) was removed via centrifugation with a molecular weight column filter (MWCO: 30 kDa; GE Vivaspin 500). Labeling yields of >85% were achieved as monitored through radioinstant thin layer chromatography (iTLC, MiniScan, Eckert and Ziegler) within 1 hour. A radiochemical purity of >98% was obtained after filtration based on iTLC. Specific activities of 4.20 ± 0.12 mCi/mg for ^{89}Zr-anti-IFNγ and 3.98 ± 0.08 mCi/mg for ^{89}Zr-anti-CD3 were achieved.

PET imaging

Tumor-bearing animals were injected i.v. with the radiolabeled antibody (~180–240 μCi/mouse, 42.8–57.1 μg in 150 μL sterile saline) in the lateral tail vein. Imaging was acquired from 4 to 72 hours post injection (p.i.). The animals were anesthetized with 3% to 5% isoflurane (Baxter Healthcare) in air for induction, then lowered to 1.5% to 2% for maintenance. Images were acquired with a microPET R4 camera (Siemens Medical Solutions, USA, formerly Concorde Microsystems). Manually drawn three-dimensional volumes of interest (VOI) were selected to determine maximum and mean percent injected dose per gram (%ID/g) in various tissues. Images were decay-corrected to the time of injection and analyzed for tracer uptake using ASIpro VMTM software v. 6.3.3.0.

In vivo treatment with CpG-ODN and monitored by IFNγ PET

IFNγ was systemically induced in naïve BALB/c mice by intramuscular (i.m.) injection of 100 μg CpG-ODN (Integrated DNA Technologies). Within an hour of treatment, the mice were injected with ^{89}Zr-anti-IFNγ in the lateral tail vein (180–240 μCi/mouse, 49.9 ± 7.2 μg). PET imaging was conducted at 72 hours p.i. Tracer uptake within the spleen and peripheral immune tissues were analyzed and compared against a control, untreated group.

Biodistribution and competitive inhibition blocking assay

Mice were injected i.v. in the lateral tail vein with ^{89}Zr-anti-IFNγ (20–30 μCi, 4.7–7.1 μg) in 100 to 150 μL saline, followed by euthanasia via CO_2 asphyxiation after 72 hours p.i., the time point identified at which tumor to background is sufficient. For blocking studies, 80 μg of cold AN-18 was coinjected with the probe in a separate cohort of mice. Select organs were harvested after sacrifice, weighed, and measured for bound radioactivity with a gamma counter (Perkin Elmer 2480 Wizard 2). The %ID/g was calculated as the percentage of activity bound to the tissue normalized against total administered activity per gram of tissue weight.

In vitro ^{89}Zr-anti-IFNγ internalization assay

TUBO cells (4.5×10^5) were plated into 6-well plates in triplicate and allowed to adhere overnight. In separate wells, cells were either left untreated or incubated with recombinant IFNγ (10 ng/mL) for 15 minutes before 3 PBS washes. ^{89}Zr-anti-IFNγ (150 ng, 0.63 nCi) was added, and cells were incubated for 1 hour at 37°C. Following the incubation period, the media were collected, and the cells were rinsed with PBS twice. Surface-bound activity was removed by washing with 100 mmol/L acetic acid + 100 mmol/L glycine (1:1, pH 3.5) at 4°C. The cells were then lysed with 1 mol/L NaOH. Each fraction was measured for activity using a gamma counter (Perkin Elmer). The %-internalized activity was calculated as the ratio of bound activity in lysates to the total activity collected from washes per well, normalized to the number of cells.

Tumor inoculation

The neu$^+$ TUBO line cloned from a spontaneous mammary tumor in a female NeuT mouse was obtained through Dr. Guido Forni (University of Torino, Torino, Italy; ref. 25). Mice were inoculated in the #4 mammary fat pad with 2.5 x 10^5 tumor cells. Tumor growth was monitored by palpation and caliper measurement. Tumor volume was calculated as $v = (l \times w^2)/2$.

DNA vaccination

The HER2/neu DNA vaccine consists of 20 μg of pGM-CSF (encoding murine GM-CSF) and 50 μg pE2TM (encoding the extracellular and transmembrane regions of human HER2) in 50 μL PBS, which is injected i.m. into each gastrocnemius followed immediately by application of electrode gel and square wave electroporation using a BTX830 (BTX Harvard Apparatus; ref. 26). For NeuT vaccination, mice were depleted of Tregs by i.p. injection of 500 μg anti-CD25 mAb PC61 10 days prior to the first vaccination.

Quantitative real-time PCR

Tumor tissue was snap frozen in liquid nitrogen. Total tumor RNA was collected by Trizol preparation (Thermo Fisher) after homogenization. cDNA was synthesized with ProtoScript II reverse transcriptase (New England Biolabs). Real-time qPCR was conducted with iTaq Universal SYBR Green Supermix (Bio-Rad Laboratories) using 10 ng cDNA/well and 500 nmol/L primers specific to the indicated gene (Life Tech). Primer sequences are found in Supplementary Table S1. Relative mRNA quantities are calculated by $2^{-\Delta CT}$ compared with GAPDH.

ELISA

Tumor tissue was homogenized in standard RIPA buffer with protease inhibitor cocktail (Sigma-Aldrich). Protein concentration

was measured by BCA assay (Thermo Fisher). High protein-binding plates (Thermo Fisher) were coated with 3 μg/mL anti–mouse-IFNγ mAb clone AN-18 (eBioscience) in coating buffer (0.1 mol/L Na_2HPO_4, pH to 9.0) and washed prior to addition of samples or standard curve using recombinant mouse IFNγ (Peprotech) in duplicate. IFNγ was detected with biotin-conjugated anti-mouse IFNγ clone R4-6A2 (eBioscience), avidin-HRP (Thermo Fisher), and TMB substrate (Thermo Fisher).

Serum IgG measurement

Serum HER2- and neu-specific IgG were quantified by flow cytometry with a BD FACSCanto II flow cytometer (Becton Dickinson), using HER2-overexpressing SKOV3 cells or neu-transfected 3T3/NKB cells as previously described (27). Regression analysis was conducted using standard curves of anti-HER2 mAb TA-1 (Calbiochem) or anti-neu mAb 7.16.4 (Calbiochem).

IFNγ ELISPOT

HER2- and neu-specific IFNγ production was measured by ELISPOT assay as previously described (27). Recombinant HER2 or neu (10 μg/mL; Sino Biologicals) were incubated with splenocytes for 48 hours in round-bottom wells, followed by transfer to anti–IFNγ-coated (clone AN-18; eBioscience) ELISPOT plates (Millipore Sigma) for an additional 48 hours. Spots were detected by biotinylated anti-IFNγ (clone R4-6A2; eBioscience) and avidin-HRP (Becton Dickinson), followed by enumeration with an ImmunoSpot analyzer (Cellular Technology Limited). Results are expressed as spot-forming units per 10^6 cells.

Treatment with anti-neu mAb 7.16.4

Mice bearing TUBO tumors were injected i.p. 5 times every 3 to 4 days with sterile-filtered ascites containing 1 mg anti-neu mAb 7.16.4 diluted in PBS to a final volume of 300 μL.

Immunohistochemistry and hematoxylin and eosin staining

IHC was performed using an anti-CD8 antibody (1:200, clone D4W2Z; Cell Signaling Technology). After euthanasia, tumors were harvested, formalin fixed, and embedded in paraffin. Note that 4 μm sections were cut using a Sakura Accu-Cut SRM microtome (Catalog#: SRM- 200 CV) and adhered onto positively charged slides (Histomax Plus, VWR). Slides were then incubated for 12 minutes at 65°C and deparrafinized in washes of xylene and graded alcohols. For IHC, antigen retrieval was performed in PT module buffer (TA-250-PM4X; Fisher), and primary antibody incubation was performed for 1 hour at room temperature in a humidified chamber. Secondary antibody incubations and DAB were performed following the manufacturers' protocols. CD8 T-cell enumeration was conducted by a blinded board-certified pathologist. Each tumor sample was screened for hotspots of CD8 lymphocytes using a Nikon Eclipse Ci microscope at 100× magnification. The number of $CD8^+$ T lymphocytes was counted in three regions with the highest infiltration at 400× magnification with a 0.55 mm field diameter, and an average was calculated. For hematoxylin and eosin staining, washed tissue sections were stained with hematoxylin (TA-125-MH; Fisher) for 5 minutes, rinsed with an acid wash for 1 minute followed by treatment with Shandon Bluing Reagent (Thermo Scientific) for 15 seconds. Eosin staining was applied to slides for 1 minute, and slides were rinsed in 95% ethanol 3 times. Sections were then dehydrated using a series of graded alcohol and xylenes washes for mounting on slides with Permount (UN1294; Fisher). Images were taken with a Spot Idea camera using Spot 5.2 software (Spot).

Tumor dissociation and flow cytometry

TUBO tumors from untreated BALB/c mice were dissociated using the GentleMACs dissociator and mouse tumor dissociation kit (Miltenyi) following the manufacturer's protocol. Cells were stained with a combination of either: FITC-conjugated CD45 mAb (clone 30-F11), APC-conjugated TCRβ mAb (clone H57-597), and eFluor780-conjugated viability dye or FITC-conjugated CD45 mAb (clone 30-F11), PE-Cy7–conjugated CD8 mAb (clone 53-6.7), APC-conjugated PD-1 mAb (J43), and eFluor780-conjugated viability dye. All antibodies/dyes were purchased from eBioscience. Samples were analyzed on a BD FACSCantoII flow cytometer (Becton Dickinson), and samples were gated on the viable fraction.

Statistical analyses

Statistical analyses were conducted using GraphPad Prism 7.02. Data shown are presented as mean ± SD. All tests use one-way ANOVA (estimating a different variance for each group) with Tukey posttest unless otherwise noted. Weekly tumor growth rate for each mouse was calculated by regression analysis of log tumor growth from day 14, when T cells become active after the initial vaccination, until the final measurement on day 38, versus time in weeks. The relationship between the estimated growth rate per week (slope from the regression analysis) for each mouse and the ^{89}Zr-anti-IFNγ tracer uptake measured at day 28 was assessed using Pearson correlation. *, $P < 0.05$; **, $P < 0.01$; and ***, $P < 0.001$.

Results

^{89}Zr-anti-IFNγ PET tracer identifies localized IFNγ production

The rat mAb AN-18 to murine IFNγ was labeled with ^{89}Zr using desferrioxamine as the chelate (^{89}Zr-anti-IFNγ) in good yields and purities according to previously reported methods (23). In mice treated with CpG-ODN to stimulate IFNγ, whole-body PET images were acquired at 72 hours p.i., a time point identified to exhibit reliable tracer uptake in the tumor, with low liver and blood pool background (Supplementary Figs. S1 and S2). VOIs drawn on splenic tissues demonstrated higher tracer accumulation (3.50 ± 0.61 %ID/g, $n = 3$) in CpG-ODN–treated groups compared with untreated controls (Ctrl: 0.83 ± 0.12 %ID/g, $n = 3$; Fig. 1A).

Tissue distribution of ^{89}Zr-anti-IFNγ at 72 hours p.i. demonstrated 20.04 ± 12.2 %ID/g uptake in the spleen (Fig. 1B; Supplementary Table S2). Uptake within the blood circulation (0.67 ± 0.69 %ID/g), as well as tissues responsible for excretion such as the liver (9.77 ± 9.12 %ID/g) and kidneys (3.93 ± 0.6 %ID/g), was low. There was also low uptake in the bone and muscle. We further confirmed specificity through competitive binding experiment where we observed a decrease in spleen uptake (20.04 ± 12.20 vs. 1.88 ± 2.74 %ID/g, $n = 4$, $P = 0.0061$) with 10× cold mAb blockade, consequently increasing nonspecific tissue accumulation in the blood (19.46 ± 12.69 %ID/g, $P = 0.0043$), heart (10.57 ± 8.91, $P = 0.30$), and liver (11.69 ± 9.82 %ID/g, $P = 0.99$). Notable differences in splenic uptake in the imaging and tissue distribution (10-fold lower mass) are due to "mass effects," wherein a greater mass of protein administered potentially saturated receptor binding sites and rendered slower pharmacokinetics (28).

Because IFNγ is a soluble protein, we sought to determine the mechanism of localized IFNγ imaging. Plated TUBO tumor cells

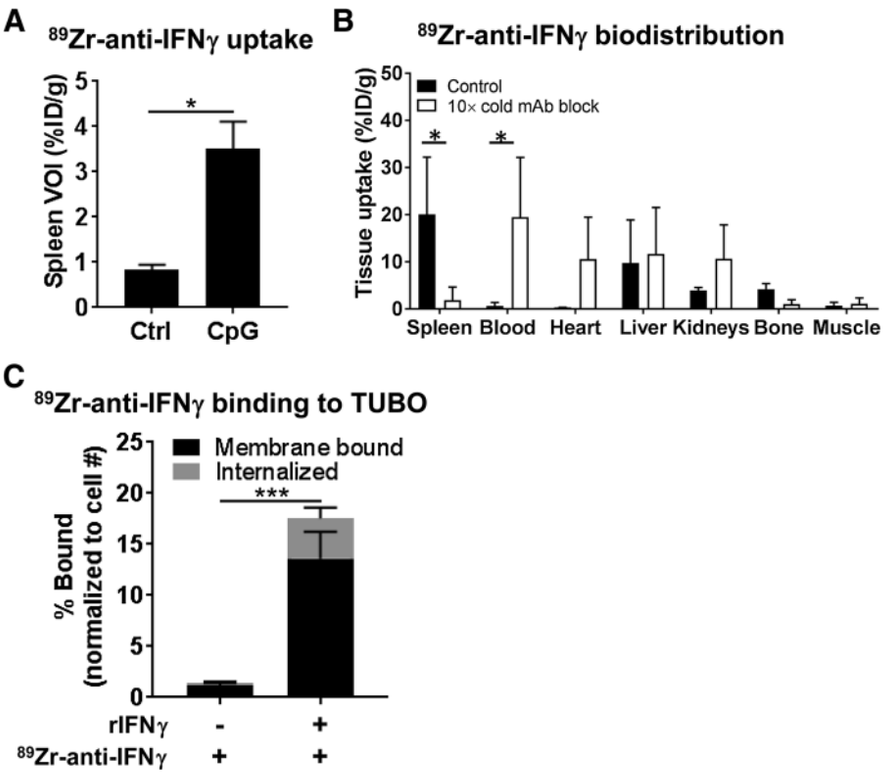

Figure 1.
Validation of specificity of ^{89}Zr-anti-IFNγ. **A,** BALB/c mice treated with CpG-ODN and imaged with the tracer 72 hours p.i. displayed higher uptake in the spleen compared with control (Ctrl)-untreated cohorts ($n = 3$ each). **B,** Tissue distribution of ^{89}Zr-anti-IFNγ at 72 hours p.i. demonstrated lower probe accumulation in the spleen upon competitive saturation with 10× cold AN-18 mAb ($n = 4$ each). **C,** Binding of ^{89}Zr-anti-IFNγ receptor-localized IFNγ was tested *in vitro*. TUBO cells were incubated with ^{89}Zr-anti-IFNγ alone ($n = 5$) or with recombinant IFNγ (rIFNγ) and washed before addition of ^{89}Zr-anti-IFNγ ($n = 5$). Activity was measured by a gamma counter and adjusted for cell count. *, $P < 0.05$; ***, $P < 0.001$.

were exposed to IFNγ and/or ^{89}Zr-anti-IFNγ tracer in quintuplicate followed by analysis of membrane binding and internalization (Fig. 1C). TUBO cells incubated with^{89}Zr-anti-IFNγ alone show limited tracer surface binding (1.13 ± 0.28%) and internalization (0.29 ± 0.13%). When TUBO is preincubated with IFNγ, enhanced ^{89}Zr-anti-IFNγ surface binding (13.62 ± 2.60%) and internalization (3.93 ± 1.07%) are observed (membrane: $P =$ 0.00039, internalized: $P = 0.0015$). Detection of tracer binding to TUBO cells after IFNγ exposure suggests localized imaging may be due to sequestration of IFNγ on its receptor *in vivo*.

IFNγ PET detects active antitumor immunity *in situ* in a syngeneic tumor model

To test the capacity of ^{89}Zr-anti-IFNγ as a noninvasive measure of antitumor immune response, neu$^+$ TUBO tumor–bearing BALB/c mice were imaged after receiving two rounds of HER2/neu DNA vaccination as detailed in Fig. 2A. This vaccine induces HER2-specific humoral and T-cell responses and approximately 10% equivalent of crossreactive anti-neu T cells without cross-reactive neu-specific antibody (26). Tumor volumes began to stabilize or regress within 1 week after the second vaccination compared with untreated TUBO-bearing mice (Fig. 2A). Control tumors were imaged a week earlier to match tumor volumes between control and vaccinated cohorts, and to prevent potential necrosis in the control tumors at the time of imaging. Mice were injected with ^{89}Zr-anti-IFNγ tracer for PET imaging (Fig. 2B; Supplementary Fig. S3A) at 72 hours p.i. A nearly 2-fold increase in tumor uptake was observed in vaccinated (Vx: 10.07 ± 1.50 %ID/g, $n = 6$) versus control mice (Ctrl: 5.97 ± 0.61 %ID/g, $n = 6$, $P = 0.0001$). A ^{89}Zr-labeled rat IgG isotype control tracer demonstrated similar tumor accumulation (72 hours p.i.) in both untreated control (5.27 ± 0.79 %ID/g) and vaccinated (5.93 ± 0.85 %ID/g) mice. This suggests baseline intratumoral IFNγ levels are low without treatment. The notable low accumulation of the isotype control tracer after vaccination supports the specificity of the IFNγ tracer and suggests increased ^{89}Zr-anti-IFNγ uptake is not simply due to vascular permeability and retention effects after ITx.

Detection of tumor-infiltrating lymphocytes via CD3 immunoPET

Total T-cell presence in the tumor microenvironment was assessed in separate groups of mice via immunoPET imaging of CD3$^+$ tumor-infiltrating lymphocytes using ^{89}Zr-anti-CD3 (Fig. 2C; Supplementary Fig. S3B). Vaccinated tumors exhibited a modest, insignificant increase of CD3 tracer binding compared with control (Vx: 6.25 ± 0.37 %ID/g, $n = 6$ vs. Ctrl: 4.58 ± 0.83 %ID/g, $n = 5$, $P = 0.16$). Both cohorts failed to demonstrate a significant change in uptake compared with Armenian hamster isotype control IgG [5.90 ± 1.26 %ID/g, $n = 3$, $P = 0.87$ (Ctrl), $P =$ 0.49 (Vx)]. Untreated TUBO tumors have endogenous T-cell infiltrates as detected by flow cytometry upon dissociation (Supplementary Fig. S4A). However, CD3 immunoPET suboptimally detected these TILs in both untreated and vaccinated mice with measured VOIs similar to the nonspecific IgG tumor accumulation. This may be due to excessive uptake by the spleen, a T-cell–homing secondary lymphoid tissue (Ctrl: 17.06 ± 3.56 %ID/g, Vx: 18.36 ± 1.49 %ID/g; Supplementary Fig. S4B), which can act as a tracer "sink." In contrast, limited splenic accumulation was observed with the IFNγ PET probe (Ctrl: 3.58 ± 0.81 %ID/g, $P < 0.0001$, Vx: 4.97 ± 0.97 %ID/g, $P < 0.0001$).

Ex vivo validation via IHC, qPCR, and ELISA

Upon completion of imaging, tissues were collected for *ex vivo* validation. Tumor tissue was assessed to verify CD3$^+$ and

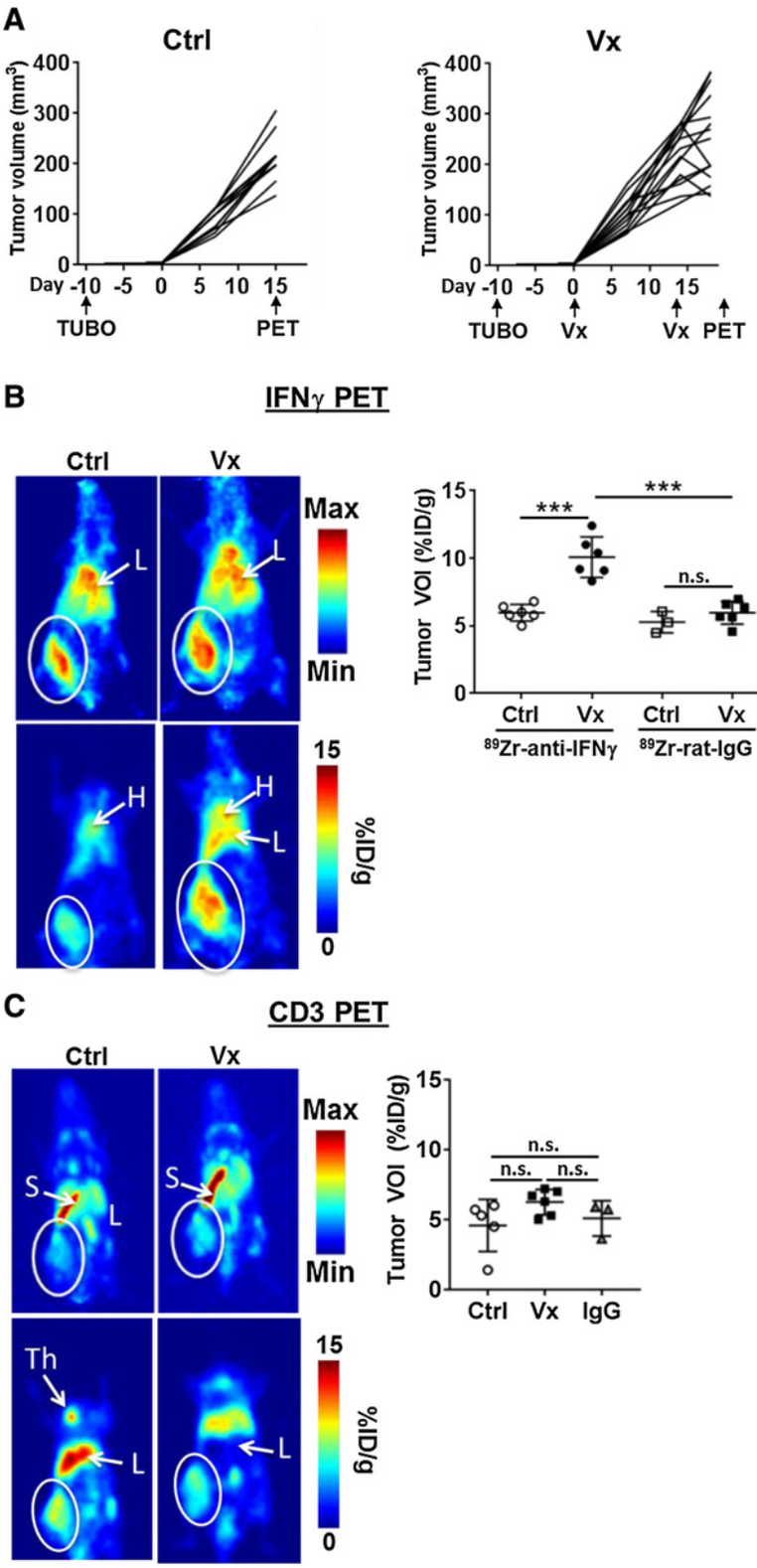

Figure 2.
PET evaluation of immunotherapy response in orthotopic TUBO mammary tumors. **A,** Tumor volume was monitored in both untreated control (Ctrl; $n = 11$; left) and vaccinated (Vx; $n = 12$; right) tumors. TUBO cells were inoculated 10 days prior to the start of vaccinations, given on days 0 and 14. PET imaging was conducted on days 15 (Ctrl) and 21 (Vx). **B,** Representative whole body maximum intensity projections (top row) and planar (bottom row) images of control (left plots; $n = 6$) and vaccinated (right plots; $n = 6$) mice with ^{89}Zr-anti-IFNγ tracer (left). White circle, tumor; L, liver; H, heart; S, spleen; Th, thymus. Tumor VOIs were measured for each mouse with a ^{89}Zr-labeled rat IgG isotype control included for each treatment group ($n = 3$, untreated control; $n = 6$, vaccinated control). **C,** Maximum intensity projection image (top plots) and planar sections (bottom plots) of ^{89}Zr-anti-CD3 images in control (left; $n = 5$) and vaccinated mice (middle; $n = 6$). A nonspecific ^{89}Zr-labeled Armenian hamster IgG isotype control was used to measure tumor VOI in a separate group of untreated mice (right, $n = 3$). ***, $P < 0.001$; n.s., not significant.

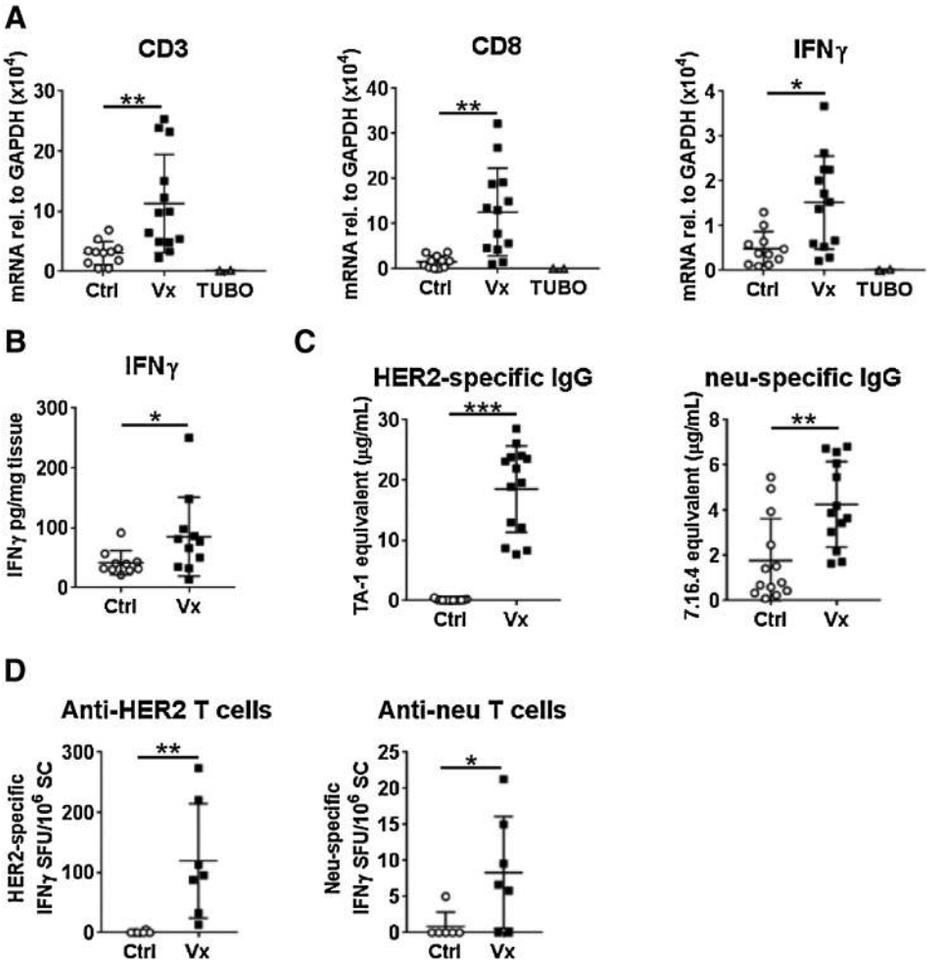

Figure 3.

Ex vivo validation of immunotherapy response in TUBO-bearing mice. Tumors were removed after imaging and validated. **A,** Total RNA obtained from control (Ctrl; $n = 11$) and vaccinated (Vx; $n = 13$) tumor tissue was analyzed by qPCR with primers specific to CD3 (left), CD8 (middle), and IFNγ (right). Cultured TUBO cells served as control ($n = 2$). **B,** IFNγ ELISA was conducted with protein lysates of TUBO tumor segments of control ($n = 10$) and vaccinated ($n = 11$) mice. **C,** HER2 and neu-specific IgG were measured in serum by flow cytometry (Ctrl, $n = 13$; Vx, $n = 14$). **D,** HER2 and neu-responsive T cells were measured by IFNγ ELISPOT (Ctrl, $n = 6$; Vx, $n = 7$). *, $P < 0.05$; **, $P < 0.01$; ***, $P < 0.001$.

$CD8^+$ T-cell presence, as well as expression of IFNγ. Transcripts levels of CD3, CD8, and IFNγ were increased in tumor tissue after vaccination (Fig. 3A; Ctrl: $n = 11$, Vx: $n = 13$), in concordance with the PET imaging data. Cultured TUBO cell cDNA is included as a negative control. CD3 and CD8 proteins were increased after treatment (Supplementary Fig. S5), and intratumoral IFNγ protein was also confirmed and quantitated by ELISA (Fig. 3B). ELISA results showed higher total IFNγ in Vx ($n = 11$) versus Ctrl ($n = 10$) TUBO tumors (Vx: 85.37 ± 65.89 vs. Ctrl: 41.69 ± 20.12 pg/mg tissue, $P = 0.043$).

Peripheral vaccine-induced immunity was measured by HER2/neu-specific serum IgG (Fig. 3C) and splenic T-cell responses (Fig. 3D). HER2-specific IgG was only detected in vaccinated mice (18.68 ± 7.40 μg/mL, $n = 14$, $P < 0.0001$). TUBO tumors constitutively express the cell surface oncogene neu, which is foreign in wild-type BALB/c mice. Neu-specific IgG is detected in unvaccinated control TUBO-bearing mice (1.58 ± 1.60 μg/mL, $n = 13$), which is further increased in vaccinated animals (6.18 ± 7.34 μg/mL, $n = 14$, $P = 0.0019$). Although the HER2 DNA vaccine itself does not induce anti-neu IgG (26), tumor cell killing likely enhanced immune activity to this foreign antigen. Detection of HER2-specific IFNγ-producing T cells was restricted to vaccinated mice, similar to anti-HER2 IgG [$119.40 \pm 95.18/10^6$ splenocytes (SC), $n = 7$, vs. $0.83 \pm 2.04/10^6$ SC in untreated controls, $n = 6$, $P = 0.0012$]. Peripheral anti-neu T cells were detected in all vaccinated animals ($8.33 \pm 7.75/10^6$ SC), whereas only 1 of 4 untreated controls showed T-cell responsiveness to neu ($0.83 \pm 2.04/10^6$ SC, $P = 0.033$). The absolute quantities of HER2 and neu-specific IgG and T cells were approximately 10-fold lower than similarly vaccinated nontumor-bearing mice (26). This may be due to tumor-associated immune suppression by myeloid-derived suppressor cells or regulatory T cells (Treg), which are reportedly increased in TUBO-bearing mice (26, 29, 30).

Detection of ITx response in a spontaneous tumor model

We next tested the capacity of IFNγ PET imaging to detect antitumor immune activity in a spontaneous tumor setting. Neu transgenic (NeuT) mice are engineered to express a transforming rat neu under the mouse mammary tumor virus promoter (22), allowing immune system recognition of neu as a self-antigen (26). We conducted our studies in male NeuT mice, which develop 1 to 2 spontaneous neu^+ salivary tumors between 30 and 40 weeks of age (22). Once tumors were palpable, Tregs were depleted using anti-CD25 mAb clone PC61 to enhance ITx response owing to the fact that NeuT mice are immune tolerant to rat neu (26, 31); this was followed by two HER2/neu DNA vaccinations as detailed in Fig. 3A. Vaccination of NeuT mice ($n = 7$) controlled tumor growth rate compared with untreated ($n = 6$) tumor-bearing NeuT mice (Fig. 4A, $P = 0.032$). IFNγ PET of vaccinated tumors displayed a nearly 2-fold higher uptake of

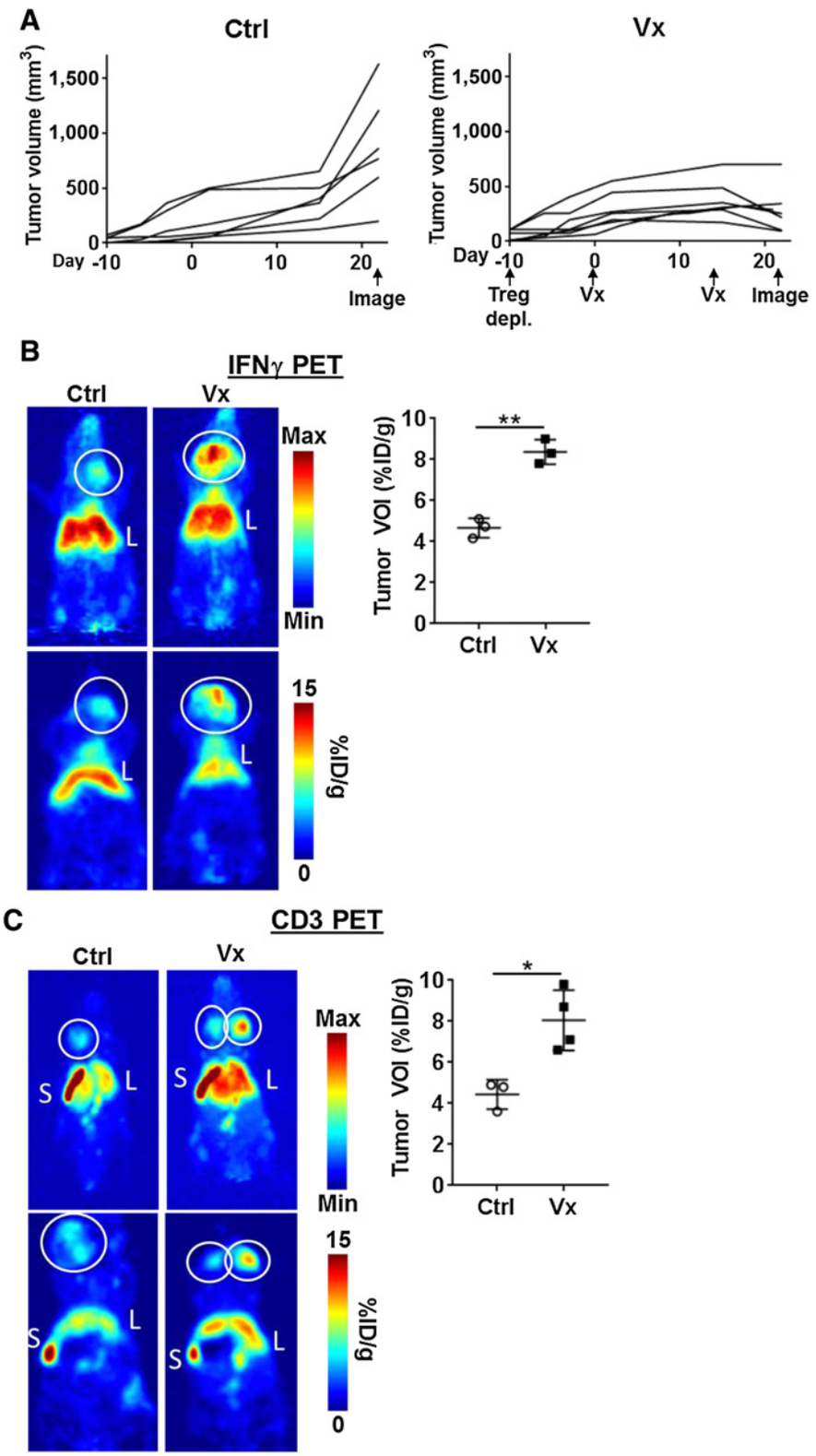

Figure 4.
PET detection of antitumor immunity in spontaneous tumor-bearing NeuT mice. **A,** Control, untreated mice (Ctrl, $n = 6$) were imaged by PET after palpable tumors were permitted to grow 31 days. For vaccinated mice (Vx, $n = 7$), upon detection of palpable spontaneous salivary tumors, Tregs were depleted 10 days prior to the first vaccination. Mice received two HER2/neu DNA vaccinations 14 days apart. PET imaging was conducted 7 days after the final vaccination. **B,** Representative whole body maximum intensity projections (top row) and planar (bottom row) images of control (left plots; $n = 3$) and HER2/neu DNA-vaccinated (right plots; $n = 4$) mice with ^{89}Zr-anti-IFNγ tracer (left). White circle, tumor; L, liver; S, spleen. Tumor VOIs were calculated for each mouse. **C,** Representative CD3 PET images of maximum intensity projections (top) and planar sections (bottom) are shown for control (left) versus vaccinated groups (right). *, $P < 0.05$; **, $P < 0.01$.

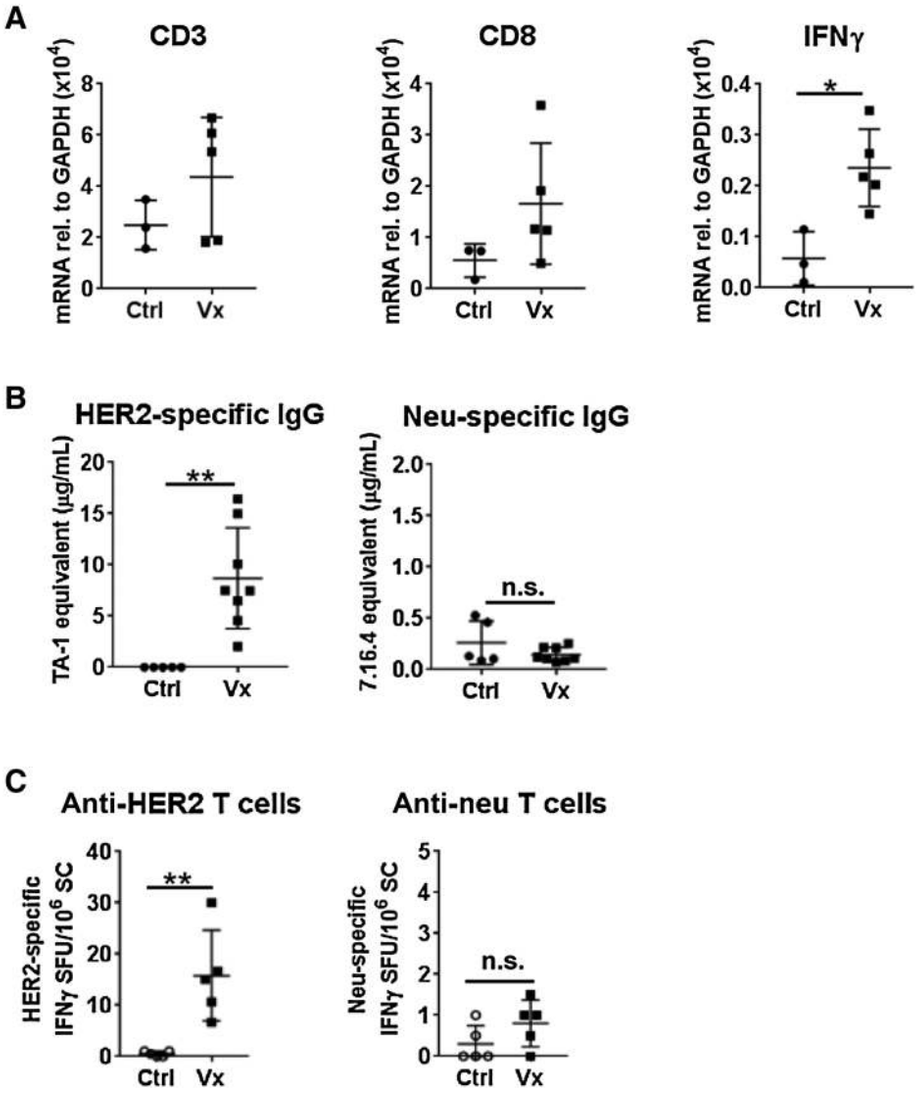

Figure 5.

Ex vivo validation of antitumor immunity in spontaneous tumor-bearing NeuT mice. **A,** Total RNA was isolated from tumor tissue, and qPCR analysis for CD3, CD8, and IFNγ was conducted (Ctrl, $n = 3$; Vx, $n = 5$). **B,** Serum HER2 (Ctrl, $n = 5$; Vx, $n = 8$) and neu-specific IgG (Ctrl, $n = 5$; Vx, $n = 8$) were measured by flow cytometry. **C,** HER2 and neu-responsive T cells were measured by IFNγ ELISPOT ($n = 5$ each). *, $P < 0.05$; **, $P < 0.01$; n.s., not significant.

^{89}Zr-anti-IFNγ (8.37 ± 0.35 %ID/g, $n = 4$) vs. control (4.63 ± 0.47 %ID/g, $n = 3$, $P = 0.001$), indicating infiltration of functional antitumor T cells (Fig. 4B; Supplementary Fig. S6A). An examination of tumor infiltrates via CD3 PET (Fig. 4C; Supplementary Fig. S6B) revealed a similar trend (Vx: 8.05 ± 1.47 %ID/g vs. Ctrl: 4.43 ± 0.72 %ID/g, $n = 3$ per group, $P = 0.012$).

Validation of T-cell infiltration and IFNγ production was conducted by qPCR in tumor tissue samples (Fig. 5A). CD3 and CD8 detection showed a variable modest, insignificant increase after vaccination, whereas IFNγ mRNA increased (Ctrl: $n = 3$, Vx: $n = 5$, $P = 0.036$). Peripheral immune response to the vaccine was evaluated by measuring serum anti-HER2 and anti-neu IgG, as well as spleen-resident HER2- and neu-responsive IFNγ-producing T cells. Tolerance to HER2/neu in NeuT mice was apparent with a comparatively lower ITx response versus wild-type BALB/c mice bearing TUBO tumors in Fig. 2. HER2-specific IgG was detected in vaccinated animals (Fig. 5B, Vx: 8.7 ± 4.9 μg/mL, $n = 8$, $P = 0.0016$ vs. Ctrl, $n = 5$), whereas anti-neu IgG was negligible or absent in all samples tested. Despite increased intratumoral detection of IFNγ in vaccinated NeuT mice by PET, peripheral T-cell response to neu was low (Fig. 5C, 15.80 ± 8.84/10^6 SC, $n = 5$) with HER2 vaccination, and was not significantly increased relative to untreated control ($n = 5$, $P = 0.27$). T-cell response to the cognate vaccine antigen was evident in anti-HER2 T cells (15.80 ± 8.84/10^6 SC, $n = 5$, $P = 0.0079$). The ratio of anti-neu to anti-HER2 T cells detected was approximately 5.1% in NeuT mice, which is 2-fold lower relative to that detected in nonimmune-tolerant BALB/c mice bearing TUBO (10.0%, Fig. 3D). These results support the hypothesis that peripheral immune monitoring may be an inadequate measure of antitumor immunity with tumor-responsive T cells preferentially localizing within the tumor, supporting the use of *in situ* analysis methods such as PET imaging.

IFNγ PET imaging is an indicator of immune activation status *in situ*

To test the capacity of ^{89}Zr-anti-IFNγ to predict treatment outcomes, BALB/c mice ($n = 11$) bearing variably sized TUBO tumors were treated with our HER2 vaccine as described previously, resulting in a range of growth slopes (Fig. 6A).

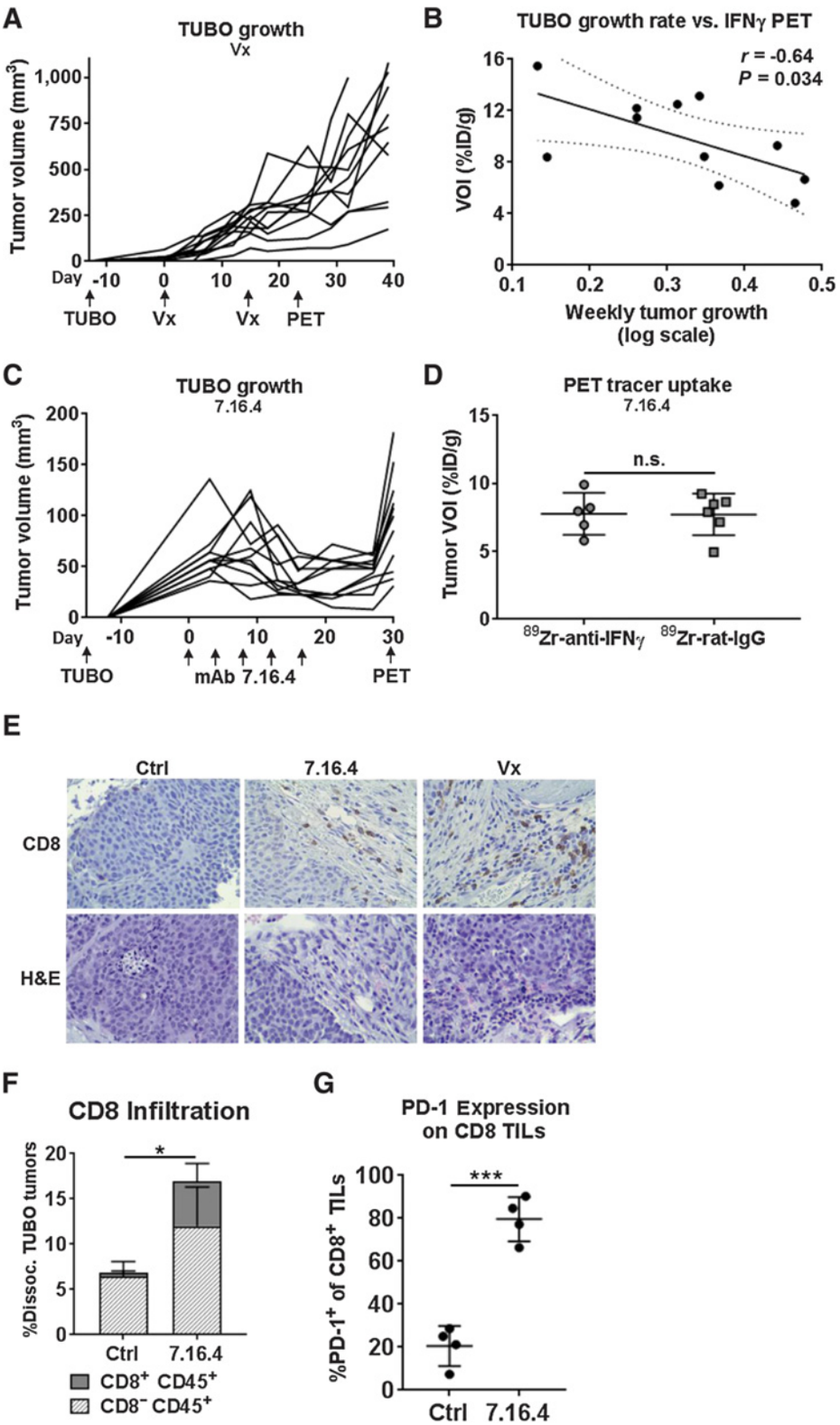

Figure 6.

IFNγ PET depicts response to ITx. **A,** Tumor volume was monitored in TUBO-bearing vaccinated (Vx) BALB/c mice ($n = 11$). TUBO cells were inoculated 13 days prior to the start of vaccinations to allow for variability in tumor volumes at treatment onset. Vaccines were given on days 0 and 14. PET imaging was conducted on day 28. **B,** Weekly tumor growth rate, calculated by regression analysis of log tumor growth, versus ^{89}Zr-anti-IFNγ tracer uptake was plotted for each mouse and evaluated by Pearson correlation. **C,** Tumor growth was monitored during passive immunotherapy with anti-neu mAb 7.16.4, given as 5 doses at 1.5 mg i.p. every 3 to 4 days as indicated, beginning 15 days after tumor inoculation. ^{89}Zr-anti-IFNγ ($n = 5$) or ^{89}Zr-rat-IgG control ($n = 6$) PET imaging was conducted 30 days after treatment onset. **D,** Tumor VOIs were calculated for ^{89}Zr-anti-IFNγ or ^{89}Zr-rat-IgG tracers in 7.16.4-treated TUBO-bearing mice. **E,** Intratumoral localization of CD8 was analyzed by IHC on formalin-fixed paraffin-embedded tissue (400×). Hematoxylin and eosin (H&E) sections are included. **F,** Control- and 7.16.4-treated tumors ($n = 4$ each) were dissociated and analyzed for T-cell infiltration by flow cytometry by staining for CD45 and CD8. **G,** PD-1 expression was analyzed by flow cytometry on CD8$^+$ tumor infiltrates from **F**. *, $P < 0.05$; ***, $P < 0.001$; n.s., not significant.

^{89}Zr-anti-IFNγ PET imaging was conducted 2 weeks after the final vaccination, and tumor volume was monitored for an additional 10 days. Tumor-localized ^{89}Zr-anti-IFNγ tracer uptake inversely correlated with tumor growth rate [Fig. 6B; Supplementary Fig. S7; $r = -0.64$; 95% confidence interval, −0.90, −0.06; $P = 0.034$], suggesting IFNγ PET is an indicator of the effects of ITx on these tumors.

We next evaluated IFNγ PET in a setting where tumor-infiltrating T cells are present but have become exhausted. TUBO-bearing mice were treated with passive ITx, using mAb 7.16.4 to rat neu. This mAb has been shown to inhibit neu signaling in addition to initiating host antitumor immunity (32, 33). Once tumors were established at approximately 50 mm^3, 1 mg doses of 7.16.4 were given i.p. at 3- to 4-day intervals for a total of 5 treatments, which reduced and stabilized tumor growth (Fig. 6C). ^{89}Zr-anti-IFNγ ($n = 5$) or control IgG ($n = 6$) PET imaging was conducted on day 30 after treatment onset, at which time, tumor growth had resumed. Tumor uptake of the IFNγ tracer was indistinguishable from IgG control, suggesting a lack of immune activity (Fig. 6D). CD8 T-cell infiltration was evaluated by IHC (Fig. 6E). A blinded pathologist's enumeration of the three regions with highest infiltration was calculated, showing a 12-fold increase in CD8 T cells after 7.16.4 treatment versus control (Ctrl: 3 ± 1, 7.16.4: 36 ± 19). Vaccinated TUBO tumor had the largest detected CD8 infiltration (74 ± 25). Overall, CD8$^+$ tumor infiltration was intermittent, with high-density regions scattered among areas with no detectable CD8$^+$ TILs (Supplementary Fig. S8). We further validated CD8 T-cell infiltration after 7.16.4 therapy by flow cytometry in a parallel cohort of treated and control mice (Fig. 6F, $n = 4$ each). An overall increase in CD45$^+$ infiltrates (Ctrl: $6.84 \pm 1.85\%$, 7.16.4: $16.95 \pm 5.88\%$, $P = 0.036$) and CD8$^+$ T cells (Ctrl: $0.41 \pm 0.19\%$, 7.16.4: $4.96 \pm 1.96\%$, $P = 0.018$) was detected after mAb treatment. Interestingly, the majority of CD8$^+$ TILs expressed the T-cell exhaustion marker PD-1 (Fig. 6G, $79.7 \pm 10.3\%$) compared with control tumors ($20.5 \pm 9.3\%$, $P = 0.0001$). Collectively, these results suggest this treatment model promotes an inactive and exhausted CD8$^+$ T-cell status despite tumor infiltration, leading to reduced IFNγ production, which was detected by ^{89}Zr-anti-IFNγ PET imaging.

Discussion

Several major drawbacks to the use of general T-cell surface markers and immune checkpoint ligands for PET imaging can complicate the assessment of ITx response. T cells are densely present in normal secondary lymphoid tissues, such as the spleen, thymus, and lymph nodes, which may hinder tumor-specific T-cell imaging. Intratumoral detection of total CD3$^+$ T cells and CD8$^+$ cytotoxic lymphocytes has been shown to positively correlate with patient outcomes (34, 35). However, the chronic inflammatory tumor microenvironment promotes checkpoint molecule expression, driving cytotoxic T cells into an exhausted state with diminished effector activity. Visualizing components of checkpoint signaling axes (e.g., PD-1/PD-L1) can influence treatment decisions by selecting patients with higher likelihood of responding to checkpoint blockade (36). In general, these methods do not measure downstream effector function of cytotoxic T cells. Larimer and colleagues reported on the utility of a peptide-based imaging tracer specific for granzyme B, a cytotoxin released by activated CTL using a syngeneic colon cancer model (37). The tracer identified responders from nonresponders after mono- or combinatorial anti–CTLA-4 and anti–PD-1-targeted inhibition; however, it is unclear whether the peptide tracer (7.46 ± 2.24 μg per mouse) solicited inhibitory effects on the enzymatic activity of granzyme B. Nevertheless, the study substantiates our rationale that imaging effector molecules along the T-cell signaling axis may provide a better readout of immune response to treatment.

To the best of our knowledge, this is the first study investigating the utility of immunoPET for detecting IFNγ. In this study, we demonstrated the capabilities of IFNγ PET to measure active antitumor immunity, providing a predictive tool for noninvasive *in situ* tumor evaluation. This approach is highly specific to the tumor compared with total T-cell imaging due to the fact that IFNγ is secreted by CTLs within the tumor. Imaging CD3, on the other hand, targets the general T-cell population that are not only localized in the tumor, but also localized in other lymphoid tissues. We also find antibody-based tracers to immune cell surface molecules may create artifacts in the experimental system. Efforts to label CD8-specific full-length mAbs (clones 2.43 and nondepleting YTS-105.18) resulted in depletion of the target cell population and tracer accumulation in the kidneys with lack of secondary lymphoid tissue detection (data not shown) despite detection of CD8$^+$ tumor infiltrates by flow cytometry and IHC (Fig. 6E and F). Anti-CD3 mAb clone 2C11 is routinely utilized for its pan–T-cell receptor agonist activity, which may also potentially alter T-cell function *in vivo*. Alternatively, it is conceivable that tracers to surface receptors may antagonize signaling, which could create off-target effects. Careful selection of antibody clones or construction of antibody fragment-based tracers like the CD8 diabody generated by Tavare and colleagues (38) or the VHH probe by Rashidian and colleagues (9) may alleviate some of these factors, but thorough quality control is necessary. Tracers targeting soluble cell products may also circumvent many of these problems.

A caveat to the detection of cytokines by PET imaging is the soluble nature of these proteins. We find localization of ^{89}Zr-anti-IFNγ in the spleen after CpG-ODN treatment and in the tumor after HER2/neu vaccination, suggesting the tracer is sequestered within the tissue. We tested the ability of TUBO tumor cells to retain IFNγ:^{89}Zr-anti-IFNγ complexes *in vitro* and find maximal binding when TUBO cells are preincubated with IFNγ, supporting the working hypothesis that localized imaging is due to detection of IFNγ associated with its receptor.

Though our *ex vivo* validation showed a general trend in agreement with the PET imaging results, a direct correlation to tracer uptake is difficult to establish. These assays, similar to a biopsy, are sampling a fragment of a heterogeneous tumor, yielding opportunity for equivocal results. Further, our IHC analyses on TUBO tumors (Fig. 6E) show the tissue is nonuniform, with regions of variable CD8 T-cell infiltration after ITx ranging from moderate density to a virtual absence. For these reasons, imaging tools like immunoPET are advantageous, bridging a clinical need by providing a more comprehensive view of the entire tumor microenvironment.

Our results showed ^{89}Zr-anti-IFNγ tracer uptake can be indicative of response to therapy in both cancer vaccination and TAA-specific mAb models. Importantly, in a tumor model recapitulating resistance to passive ITx, IFNγ PET identified an inactive, dysfunctional immune system despite the presence of CD8$^+$ T-cell infiltrates. This discordance was likely due to elevated PD-1 expression as shown by flow cytometry, hindering CTLs from

productive antitumor immunity. We further demonstrated that IFNγ PET may be more sensitive for determining response to ITx when compared with peripheral immune evaluation, a point that should be evaluated further. IFNγ PET can also serve as a universal noninvasive measurement of immune activity *in situ* for a variety of cancers with virtually any ITx modality, without the need for knowledge of specific antigens or cumbersome *ex vivo* antigen recall assays. *In situ* detection of IFNγ may be a powerful tool for assessing intratumoral immune activation status, which could help distinguish between true tumor progression and pseudoprogression, where tumor volume swells as inflammatory cells infiltrate. In addition, the utility of IFNγ PET can potentially expand beyond cancer immune monitoring to include examination of localized inflammatory conditions such as injury, infection, or autoimmune disease. Taken together, these results support the development of IFNγ PET tracers for clinical evaluation of tumor ITx.

Disclosure of Potential Conflicts of Interest

No potential conflicts of interest were disclosed.

Disclaimer

The content is solely the responsibility of the authors and does not necessarily represent the official views of the NIH.

Authors' Contributions

Conception and design: H.M. Gibson, W.-Z. Wei, N.T. Viola-Villegas
Development of methodology: H.M. Gibson, B.N. McKnight, A. Malysa, W.-Z. Wei, N.T. Viola-Villegas
Acquisition of data (provided animals, acquired and managed patients, provided facilities, etc.): H.M. Gibson, C.E. McCarthy, J. Reyes, W.-Z. Wei
Analysis and interpretation of data (e.g., statistical analysis, biostatistics, computational analysis): H.M. Gibson, B.N. McKnight, G. Dyson, W.N. Wiesend, C.E. McCarthy, W.-Z. Wei, N.T. Viola-Villegas
Writing, review, and/or revision of the manuscript: H.M. Gibson, B.N. McKnight, G. Dyson, C.E. McCarthy, W.-Z. Wei, N.T. Viola-Villegas
Administrative, technical, or material support (i.e., reporting or organizing data, constructing databases): H.M. Gibson, W.N. Wiesend, J. Reyes, W.-Z. Wei, N.T. Viola-Villegas
Study supervision: H.M. Gibson, W.-Z. Wei, N.T. Viola-Villegas
Other (I wrote the methodology of my contribution for the paper): A. Malysa

Acknowledgments

The authors gratefully acknowledge the Microscopy, Imaging and Cytometry Resources Core, and the Biobanking and Correlative Sciences Core, which are supported, in part, by the NIH Center grant P30 CA022453 to the Karmanos Cancer Institute at Wayne State University. Research reported in this publication was supported by the NCI of the NIH under award numbers R00 CA181492 (N.T. Viola-Villegas), R37 CA220482 (N.T. Viola-Villegas and H.M. Gibson), R01 CA76340 (W.-Z. Wei), and NIH T32 CAA09531 (B.N. McKnight). Additional support was provided by Karmanos Cancer Institute Strategic Research Initiative Grant (H.M. Gibson and N.T. Viola-Villegas) and Wayne State University OVPR Grants Boost (H.M. Gibson and N.T. Viola-Villegas).

The costs of publication of this article were defrayed in part by the payment of page charges. This article must therefore be hereby marked *advertisement* in accordance with 18 U.S.C. Section 1734 solely to indicate this fact.

Received January 24, 2018; revised June 15, 2018; accepted August 2, 2018; published first August 16, 2018.

References

1. Restifo NP, Dudley ME, Rosenberg SA. Adoptive immunotherapy for cancer: harnessing the T cell response. Nat Rev Immunol 2012;12:269–81.
2. Kroemer G, Senovilla L, Galluzzi L, André F, Zitvogel L. Natural and therapy-induced immunosurveillance in breast cancer. Nat Med 2015;21:1128–38.
3. Kohrt HE, Tumeh PC, Benson D, Bhardwaj N, Brody J, Formenti S, et al. Immunodynamics: a cancer immunotherapy trials network review of immune monitoring in immuno-oncology clinical trials. J Immunother Cancer 2016:4:15.
4. Hoos A, Janetzki S, Britten CM. Advancing the field of cancer immunotherapy: MIATA consensus guidelines become available to improve data reporting and interpretation for T-cell immune monitoring. Oncoimmunology 2012;1:1457–9.
5. Yuan J, Hegde PS, Clynes R, Foukas PG, Harari A, Kleen TO, et al. Novel technologies and emerging biomarkers for personalized cancer immunotherapy. J Immunother Cancer 2016;4:3.
6. Chen PL, Roh W, Reuben A, Cooper ZA, Spencer CN, Prieto PA, et al. Analysis of immune signatures in longitudinal tumor samples yields insight into biomarkers of response and mechanisms of resistance to immune checkpoint blockade. Cancer Discov 2016;6:827–37.
7. Gerlinger M, Rowan AJ, Horswell S, Larkin J, Endesfelder D, Gronroos E, et al. Intratumor heterogeneity and branched evolution revealed by multiregion sequencing. N Engl J Med 2012;366:883–92.
8. Larimer BM, Wehrenberg-Klee E, Caraballo A, Mahmood U. Quantitative CD3 PET imaging predicts tumor growth response to anti-CTLA-4 therapy. J Nucl Med 2016;57:1607–11.
9. Rashidian M, Ingram JR, Dougan M, Dongre A, Whang KA, LeGall C, et al. Predicting the response to CTLA-4 blockade by longitudinal noninvasive monitoring of CD8 T cells. J Exp Med 2017;214:2243–55.
10. Natarajan A, Mayer AT, Xu L, Reeves RE, Gano J, Gambhir SS. Novel radiotracer for immunoPET imaging of PD-1 checkpoint expression on tumor infiltrating lymphocytes. Bioconjug Chem 2015;26:2062–9.
11. Truillet C, Oh HLJ, Yeo SP, Lee CY, Huynh LT, Wei J, et al. Imaging PD-L1 expression with ImmunoPET. Bioconjug Chem 2018;29:96–103.
12. Cole EL, Kim J, Donnelly DJ, Smith RA, Cohen D, Lafont V, et al. Radiosynthesis and preclinical PET evaluation of ^{89}Zr-nivolumab (BMS-936558) in healthy non-human primates. Bioorganic Med Chem 2017;25:5407–14.
13. England CG, Ehlerding EB, Hernandez R, Rekoske BT, Graves SA, Sun H, et al. Preclinical pharmacokinetics and biodistribution studies of 89Zr-labeled pembrolizumab. J Nucl Med 2017;58:162–8.
14. Kikuchi M, Clump DA, Srivastava RM, Sun L, Zeng D, Diaz-Perez JA, et al. Preclinical immunoPET/CT imaging using Zr-89-labeled anti-PD-L1 monoclonal antibody for assessing radiation-induced PD-L1 upregulation in head and neck cancer and melanoma. Oncoimmunology 2017;6:e1329071.
15. Hettich M, Braun F, Bartholomä MD, Schirmbeck R, Niedermann G. High-resolution PET imaging with therapeutic antibody-based PD-1/PD-L1 checkpoint tracers. Theranostics 2016;6:1629–40.
16. Schoenborn JR, Wilson CB. Regulation of interferon-gamma during innate and adaptive immune responses. Adv Immunol 2007;96:41–101.
17. Coussens LM, Zitvogel L, Palucka AK. Neutralizing tumor-promoting chronic inflammation: a magic bullet? Science 2013;339:286–91.
18. Li K, Baird M, Yang J, Jackson C, Ronchese F, Young S. Conditions for the generation of cytotoxic CD4+ Th cells that enhance CD8+ CTL-mediated tumor regression. Clin Transl Immunol 2016;5:e95.
19. Knutson KL, Disis ML. Tumor antigen-specific T helper cells in cancer immunity and immunotherapy. Cancer Immunol Immunother 2005;54:721–8.
20. Xu X, Fu X, Plate J, Chong AS. IFN-γ induces cell growth inhibition by fas-mediated apoptosis: requirement of STAT1 protein for up-regulation of fas and fasl expression. Cancer Res 1998;58:2832–7.
21. Zaidi MR, Merlino G. The two faces of interferon-γ in cancer. Clin Cancer Res 2011;17:6118–24.
22. Diodoro MG, Carlo E Di, Zappacosta R, Iezzi M, Coletti A, Modesti A, et al. Salivary carcinoma in HER-2/neu transgenic male mice: an angiogenic switch is not required for tumor onset and progression. Int J Cancer 2000;88:329–35.

23. Viola-Villegas NT, Sevak KK, Carlin SD, Doran MG, Evans HW, Bartlett DW, et al. Noninvasive imaging of PSMA in prostate tumors with89Zr-Labeled huJ591 engineered antibody fragments: the faster alternatives. Mol Pharm 2014;11:3965–73.
24. Viola-Villegas NT, Rice SL, Carlin S, Wu X, Evans MJ, Sevak KK, et al. Applying PET to broaden the diagnostic utility of the clinically validated CA19.9 serum biomarker for oncology. J Nucl Med 2013;54:1876–82.
25. Rovero S, Amici A, Carlo ED, Bei R, Nanni P, Quaglino E, et al. DNA vaccination against rat Her-2/Neu p185 more effectively inhibits carcinogenesis than transplantable carcinomas in transgenic BALB/c Mice. J Immunol 2000;165:5133–42.
26. Jacob J, Radkevich O, Forni G, Zielinski J, Shim D, Jones RF, et al. Activity of DNA vaccines encoding self or heterologous Her-2/neu in Her-2 or neu transgenic mice. Cell Immunol 2006;240:96–106.
27. Gibson HM, Veenstra JJ, Jones R, Vaishampayan UI, Sauerbrey M, Bepler G, et al. Induction of HER2 immunity in outbred domestic cats by DNA electrovaccination. Cancer Immunol Res 2015;3:777–86.
28. Pandit-Taskar N, O'Donoghue JA, Durack JC, Lyashchenko SK, Cheal SM, Beylergil V, et al. A phase I/II study for analytic validation of 89Zr-J591 ImmunoPET as a molecular imaging agent for metastatic prostate cancer. Clin Cancer Res 2015;21:5277–85.
29. Deng L, Liang H, Burnette B, Beckett M, Darga T, Weichselbaum RR, et al. Irradiation and anti-PD-L1 treatment synergistically promote antitumor immunity in mice. J Clin Invest 2014;124:687–95.
30. Linch SN, Kasiewicz MJ, McNamara MJ, Hilgart-Martiszus IF, Farhad M, Redmond WL. Combination OX40 agonism/CTLA-4 blockade with HER2 vaccination reverses T-cell anergy and promotes survival in tumor-bearing mice. Proc Natl Acad Sci 2016;113:E319–27.
31. Ambrosino E, Spadaro M, Iezzi M, Curcio C, Forni G, Musiani P, et al. Immunosurveillance of Erbb2 carcinogenesis in transgenic mice is concealed by a dominant regulatory T-cell self-tolerance. Cancer Res 2006; 66:7734–40.
32. Whittington PJ, Piechocki MP, Heng HH, Jacob JB, Jones RF, Back JB, et al. DNA vaccination controls Her-2+ tumors that are refractory to targeted therapies. Cancer Res 2008;68:7502–11.
33. Park S, Jiang Z, Mortenson ED, Deng L, Radkevich-Brown O, Yang X, et al. The therapeutic effect of anti-HER2/neu antibody depends on both innate and adaptive immunity. Cancer Cell 2010;18:160–70.
34. Stanton SE, Disis ML. Clinical significance of tumor-infiltrating lymphocytes in breast cancer. J Immunother cancer 2016;4:59.
35. Gooden MJM, de Bock GH, Leffers N, Daemen T, Nijman HW. The prognostic influence of tumour-infiltrating lymphocytes in cancer: a systematic review with meta-analysis. Br J Cancer 2011;105:93–103.
36. Gnjatic S, Bronte V, Brunet LR, Butler MO, Disis ML, Galon J, et al. Identifying baseline immune-related biomarkers to predict clinical outcome of immunotherapy. J Immunother Cancer 2017;5:44.
37. Larimer BM, Wehrenberg-Klee E, Dubois F, Mehta A, Kalomeris T, Flaherty K, et al. Granzyme B PET imaging as a predictive biomarker of immunotherapy response. Cancer Res 2017;77:2318–27.
38. Tavaré R, Escuin-Ordinas H, Mok S, McCracken MN, Zettlitz KA, Salazar FB, et al. An effective immuno-PET imaging method to monitor CD8-dependent responses to immunotherapy. Cancer Res 2016;76:73–82.